2023

Experimental validation of inertia parameters and attitude estimation of uncooperative space targets using solid state LIDAR

Alessia Nocerino

Roberto Opromolla

Giancarmine Fasano

Michele Grassi

Spencer John

See next page for additional authors

Authors

Alessia Nocerino, Roberto Opromolla, Giancarmine Fasano, Michele Grassi, Spencer John, Hancheol Cho, and Riccardo Bevilacqua

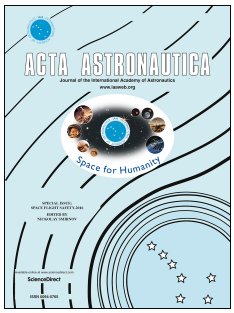

Experimental validation of inertia parameters and attitude estimation of uncooperative space targets using solid state LIDAR

Alessia Nocerino, Roberto Opromolla, Giancarmine Fasano, Michele Grassi, Pol Fontdegloria Balaguer, Spencer John, Hancheol Cho, Riccardo Bevilacqua

PII: S0094-5765(23)00060-7

DOI: https://doi.org/10.1016/j.actaastro.2023.02.010

Reference: AA 9685

To appear in: *Acta Astronautica*

Received Date: 1 February 2023

Accepted Date: 4 February 2023

Please cite this article as: A. Nocerino, R. Opromolla, G. Fasano, M. Grassi, P. Fontdegloria Balaguer, S. John, H. Cho, R. Bevilacqua, Experimental validation of inertia parameters and attitude estimation of uncooperative space targets using solid state LIDAR, *Acta Astronautica* (2023), doi: https://doi.org/10.1016/j.actaastro.2023.02.010.

Experimental validation of inertia parameters and attitude estimation of uncooperative space targets using solid state LIDAR

Alessia Nocerino, Roberto Opromolla, Giancarmine Fasano, Michele Grassi

University of Naples "Federico II", Dept. of Industrial Engineering, P.le Tecchio 80 – 80125 Napoli – Italy

Pol Fontdegloria Balaguer, Spencer John, Hancheol Cho, Riccardo Bevilacqua (corresponding author: bevilacr@erau.edu)

Embry Riddle Aeronautical University, 1 Aerospace Boulevard – Daytona Beach – FL 32114 – United States,

Abstract

This paper presents an experimental activity aimed at assessing performance of techniques for inertia and attitude parameters estimation of an uncooperative but known space target. The adopted experimental set-up includes a scaled-down 3D printed satellite mock-up, a spherical air bearing and a low-cost solid-state LIDAR. The experimental facility also comprises a motion capture system to obtain a benchmark of the pose (position and attitude) parameters and an ad-hoc designed passive balancing system to keep the centre of mass as close as possible to the centre of rotation. The LIDAR-based 3D point clouds, collected while the target rotates on the spherical air-bearing to reproduce the rotational dynamics of an almost-free rigid body, are processed to obtain pose and angular velocity estimate. Those data are used to determine the inertia properties of the target by solving a linear system based on the integral form of Euler equations. Performance and robustness of the algorithm for attitude and inertia properties estimation are assessed considering both the inertia benchmark provided by a high-fidelity CAD model of the target and the pose solution obtained from the motion tracking system and its extrinsic calibration with respect to the LIDAR.

Keywords

Inertia parameter estimation; attitude estimation; uncooperative target; solid-state LIDAR

1. INTRODUCTION

Despite the introduction of passive mitigation measures to ensure the long-term sustainability of space activities such as the Inter-Agency Space Debris Coordination Committee (IADC) Space Debris Mitigation Guidelines [1] and the ESA Space Debris Mitigation Handbook [2], many studies have highlighted the need of complementing them with the active removal of the largest debris in Earth Orbit, like defunct spacecraft and rocket bodies, in order to stabilize the growth of the debris population [3]–[5].

In Active Debris Removal (ADR) scenarios, the target is likely uncooperative, i.e., it is not able to actively or passively (e.g., through some recognizable artificial markers) communicate with the servicing spacecraft exchanging information

to safely perform the docking or berthing operations. In addition, due to the long time spent in orbit, space target shape and inertia properties may have been changed (e.g., due to fragmentation or due to the uncertain amount of propellant left on board). However, their knowledge is vital both to allow the estimate of the rotational motion during monitoring and capture phase and to control the stack in the post capture phase. Thus, the development of reliable and robust techniques to accurately reconstruct the inertia properties before performing final approach and berthing or docking operations is highly advisable. In this respect, pose data retrieved by Electro Optical sensor can be exploited to estimate the inertia properties of the target. It is worth noting that without perturbing the rotational dynamics with an external and known torque (e.g., physically impacting the target [6], or approaching it with a permanent magnet able to produce eddy currents [7]), the moments of inertia can be estimated up to a scale factor. However, apply those torques to the target implies that the chaser ha to approach closely the target to perturb it, thus risking unwanted collision and fragmentation. Hence, safer approaches should be preferred. The Moment of Inertia ratios (MIRs) can be estimated during the monitoring phase, when the two spacecraft are in a safe relative configuration, then the scale factor can be estimated once the target is captured, and the stack has been stabilized. In addition, scaled moments of inertias are sufficient to propagate the rotational dynamics of the target and predict its pose. State-of-the-art approaches for inertia properties estimation purposes relies on the conservation of the angular momentum or on the time invariance of the inertia parameters. For instance, Sheinfeld et al. describe a strategy for the estimation of both center of mass location and MIRs of a tumbling space target which exploits an unconstrained least square approach, [8]. They also identify the condition to be met which guarantees a physical solution: the angular velocity measurements involved in the MIRs determination procedure must be linearly independent. This approach has been extended in [9] to take the inequality constraints on the inertia parameters into account and to ensure positive diagonal entries in the estimated MIRs matrix by applying the active set method for convex quadratic programming. The observability of the problem is also addressed: in case of pure rotation (i.e., when the target rotates around one of the principal axis) or when the nutation angle (i.e., the angle between the angular momentum vector and the angular velocity vector) is null, the MIRs matrix is not fully observable.

Thus, the determination of the inertia properties of a non-cooperative target cannot prescind from its motion parameters estimation. These two tasks are usually carried out simultaneously within a tightly coupled relative navigation architectures fed with stereovision measurements. In this regard, [10] presents a relative navigation architecture which enables close proximity operations with non-cooperative space objects coping with uncertainties on the inertia properties of the target. The motion and inertia parameters estimations are carried out by a set of Iterative Extended Kalman Filter (IEKF) assuming different probable inertia tensor: the most probable one is determined through a Maximum A Posterior (MAP) estimator as the one corresponding to the lowest innovation variance. A similar approach in which the IEKF is substituted by a Cubature Kalman Filter is (CKF) is proposed in [11]. An adaptive Unscented Kalman Filter (UKF) which

aims at modifying the covariance of the MIRs according to the measurement updating errors of the relative state, obtaining a two-stage estimation procedures is presented in [12]. Stereo-vision measurements are also exploited in [13] to estimate both motion and state parameters of an uncooperative space target by solving an optimization problem in which the objective function is the difference between the observed and the predicted motion.

A different parametrization of the inertia parameters corresponding to the logarithm of the principal MIRs is introduced in [14]. The state and inertia parameters are estimated by solving with the Incremental Smoothing and Mapping (iSAM) a pose-graph optimization problem. The advantage of the logarithmic parametrization consists in solving the estimation problem without considering additional constraints, having the logarithm the same validity domain of the MIRs. This parametrization has been also exploited in [15] within an IEKF in which a pseudo-measurement constraints is included to force the inertia ratios to converge to the correct value. However, some major drawbacks due to overexposure or shadowing effect due to the Sun must be considered when using passive systems. On the contrary, active systems (e.g., LIDARs) guarantees robustness against the harsh illumination condition that a spacecraft may encounter on orbit. Active system measurements are usually integrated in architectures for state and inertia estimation according to a loosely-coupled configuration.

However, the use of stereo-vision systems can be effective only at very short distance (e.g., up to ten o meters) due to the limits posed on the achievable baseline by installation constraints. Alternative technological solutions to stereo systems have also been considered. In [16], the relative motion and the target inertia parameters are estimated by a two-stage algorithms which exploits the measurements of a monocular camera by minimizing the difference between the points' pixel coordinates of a set of features and the corresponding ones on the target model. Aghili and Parsa propose an EKF which estimates both the full relative motion state and the inertia parameters of the target satellite as well as the covariance of the measurement noise by exploiting the pose provided by the processing of a Laser Camera System data, [17]. The use of active systems is also foreseen in [18] where range images acquired by a set of cooperating 3D sensors are exploited for the estimate of the motion state, shape and inertia parameters of an unknown target. The same problem have been addressed in [19] in which the authors use the Iterative Closest Point (ICP) algorithm to track the pose of an uncooperative target by registering consecutive point cloud measured with a LIDAR system and estimate the target MIRs and relative motion state within an EKF settings.

Anyway, some limitations arise from the use of Kalman filters for inertia properties estimation due to the strong influence on the achievable results of the filter tuning parameters and the high sensitivity to non-Gaussian noise which usually characterize the vision-based measurements. Thus, a multi-step LIDAR-based architecture which separates the inertia properties estimation task from the relative navigation task, [20]. It first estimates the MIRs exploiting the principle

of the conservation of the angular momentum and LIDAR-based pose measurements, then track the full relative motion state by means of a UKF.

Although these works have addressed the problem of the inertia properties estimation of uncooperative target, their results are mostly based on numerical simulations. Instead, this paper tackles the problem from an experimental point of view by addressing the issue related to processing of real sensor data to estimate the attitude and the MIRs of a non-cooperative but known target.

The rest of the paper is organized as follows. Section 2 introduces the adopted mathematical notations and the definitions of applicable reference frames. Section 3 provides an overview of the pose estimation and inertia properties determination approaches experimentally assessed in this work. Section 4 describes the experimental set-up, while the testing procedure is introduced in Section 5. Section 6 presents and discusses the test results. Finally, conclusions are drawn in Section 7.

2. MATHEMATICAL FORMULATION AND REFERENCE FRAMES DEFINITION

The following mathematical notations are adopted.

- Plain italic letters (a) are used to indicate scalar quantities.
- Bold italic letters ($\boldsymbol{a}$) are used to indicate vectors.
- Double underlined capital italic letters ($\underline{\underline{A}}$) are used to indicate matrices.

Also, the position and angular velocity vectors of a reference frame B with respect to reference frame A in reference frame C are indicated with $\boldsymbol{t}_{B/A}^{C}$ and $\boldsymbol{\omega}_{B/A}^{C}$ respectively. If frame C coincides with frame A, the apex is neglected. Finally, the rotation matrix from reference A to reference B is indicated as $\underline{\underline{R}}_{A}^{B}$ and its corresponding quaternion is denoted as $\boldsymbol{q}_{B/A}$. A list of the adopted reference frames is reported below.

- The Lidar Reference Frame (LRF) is a sensor-fixed coordinate system with the origin in the sensor optical center, the z_{LRF} axis pointing along the boresight direction and the x_{LRF} and y_{LRF} axes laying on the image plane. It is worth outlining that in this case, the LRF can be considered an inertial reference frame, being fixed with respect to the ground.
- The Target Reference Frame (TRF) is a target-fixed coordinate system.
- The Motion Tracking Reference Frame (MTRF) is the one in which the motion tracking system outputs its measurements.

3. POSE ESTIMATION AND INERTIA PROPERTIES DETERMINATION

This section provides fundamentals of the approaches used to estimate both the pose (by processing the 3D point clouds acquired by the LIDAR system) and the MIRs of the target. The different processing steps that allow determining the inertia properties of the target can be summarized in the flow diagram shown in Fig. 1. First, the 3D point clouds of the observed scene are processed by a customized Iterative Closest Point (ICP) algorithm to estimate the pose. Then, the measured attitude is differentiated through a numerical method to get target angular velocity estimates. When in orbit, the relative angular velocity obtained by differentiating the estimated quaternion and the chaser inertial angular velocity must be combined to obtain the target absolute angular velocity. In the laboratory environment the LRF is an inertial frame, thus the angular velocity of the target with respect to the LIDAR can be considered an inertial velocity. Finally, the MIRs are determined by solving with a Least Square approach an overdetermined system based on the Euler equations for a free rigid body.

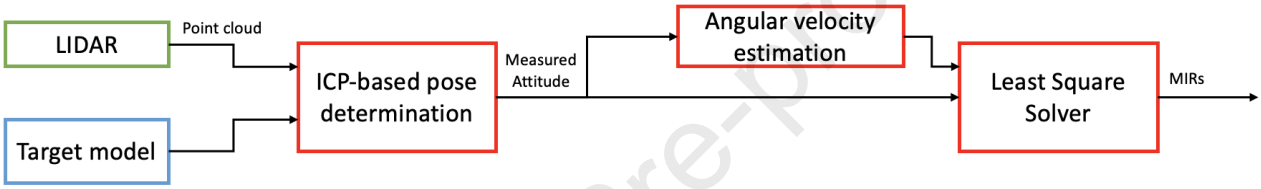

Fig. 1 Flow diagram of the MIRs estimation procedure.

3.1 ICP fundamentals

The ICP algorithm is an iterative technique which aims at finding the best roto-translation aligning two 3D datasets [21]; in this case, the LIDAR point clouds and a model point cloud (i.e., obtained from the knowledge of the target geometry). In this work, the pose is estimated by exploiting a customized version of the ICP, described in [22]. Some details are provided hereinafter.

The ICP consists in two steps: matching and registration. The former aims at finding the correspondences between the model and measured points by applying a Nearest Neighbour (NN) approach (i.e., each point of the dataset is first reprojected in TRF based on a pose initial guess and then associated to the closest point of the model). The second step aims at finding the pose parameters minimizing the mean squared distance between corresponding points, as shown in Eq. (21):

$$f(q) = \frac{1}{N_p}\sum_{i=1}^{N_p}\left|\left|\left[\boldsymbol{P}_i^{BRF} - R\left(q_{LRF/BRF}\right)^T\left(\boldsymbol{P}_i^{LRF} + \boldsymbol{T}_{BRF/LRF}\right)\right]\right|\right|^2 \tag{1}$$

where $\boldsymbol{P}_i^{TRF}$ and $\boldsymbol{P}_i^{LRF}$ are the i-th corresponding points of the model and LIDAR point cloud, respectively and N_p is the number of matched points.

This procedure is iterated until the variation of the cost function between two subsequent iterations goes below a user-defined threshold, τ_{DMS}, or a user-defined maximum number of iterations, τ_{MAX}, is reached.

The ICP-based attitude is exploited to obtain an estimate of the angular velocity of the target as follows.

The quaternion that describes the attitude variation from a time instant t to $t+\Delta t$, ($\Delta \boldsymbol{q}_{TRF/LRF}$), can be computed from the attitude measurements at t and $t+\Delta t$ by inverting Eq. (2), as in [20] and [22]:

$$\boldsymbol{q}_{BRF/LRF}(t+\Delta t) = \boldsymbol{q}_{BRF/LRF}(t) \otimes \Delta \boldsymbol{q}_{BRF/LRF} \tag{2}$$

Also, if the small angle assumption can be applied, the attitude variation $\Delta \boldsymbol{q}_{TRF/LRF}$ can be approximated as in Eq. (3)

$$\Delta \boldsymbol{q}_{TRF/LRF} \approx \begin{bmatrix} 1 \\ \frac{1}{2}\Delta \boldsymbol{\varphi} \end{bmatrix} \tag{3}$$

where $\boldsymbol{\Delta\varphi}$ is the Euler vector corresponding to $\Delta \boldsymbol{q}_{TRF/LRF}$

By definition, the angular velocity is given by Eq. (4)

$$\boldsymbol{\omega}_{TRF/LRF}^{LRF} = \frac{d\boldsymbol{\varphi}}{dt} \tag{4}$$

where $\boldsymbol{\varphi}$ is the Euler vector representation of the attitude. A first order finite difference method is applied to Eq. (4) by considering a time interval short enough to keep the small angle assumption valid. A threshold of 10° is set to the equivalent Euler angle describing the attitude change between two considered time instants to compute the angular velocity.

Finally, a low pass filter, specifically a Savitzky-Golay filter [23], is applied to the collected time-history of the target angular velocity to reduce the level of noise.

3.1 Moment of inertia ratios estimation

The rotational dynamics of a freely tumbling rigid body is described by the Euler equation in Eq. (5):

$$\underline{\underline{I}}_T \dot{\boldsymbol{\omega}}_{TRF/LRF}^{LRF} + \boldsymbol{\omega}_{TRF/LRF}^{LRF} \times \underline{\underline{I}}_T \boldsymbol{\omega}_{TRF/LRF}^{LRF} = 0 \tag{5}$$

where $\underline{\underline{I}}_T$ is the target inertia matrix.

By isolating the term $\underline{\underline{I}}_T$, Eq. (5) becomes:

$$\left[\underline{\underline{\dot{\Omega}}}_{TRF/LRF}^{LRF} + [\boldsymbol{\omega}_{TRF/LRF}^{LRF} \times] \underline{\underline{\Omega}}_{TRF/LRF}^{LRF}\right] \boldsymbol{I}_T = 0 \tag{6}$$

where

$$\boldsymbol{I}_T = \begin{bmatrix} I_{xx} & I_{yy} & I_{zz} & I_{xy} & I_{xz} & I_{yz} \end{bmatrix}^T \tag{7}$$

$$[\boldsymbol{\omega}_{TRF/LRF}^{LRF} \times] = \begin{bmatrix} 0 & -\omega_z & \omega_y \\ \omega_z & 0 & -\omega_x \\ -\omega_y & \omega_x & 0 \end{bmatrix} \tag{8}$$

$$\underline{\underline{\Omega}}^{LRF}_{TRF/LRF} = \begin{bmatrix} \omega_x & 0 & 0 & \omega_y & \omega_z & 0 \\ 0 & \omega_y & 0 & \omega_x & 0 & \omega_z \\ 0 & 0 & \omega_z & 0 & \omega_x & \omega_y \end{bmatrix} \tag{9}$$

being ω_x, ω_y and ω_z the cartesian components of $\omega^{LRF}_{TRF/LRF}$. Since the number of rows in the linear system of Eq. (6) is lower than the number of unknowns, at least three different observations must be used to find a solution. Also, since Eq. (6) is a homogenous system, its solution can be determined up to a scale factor. Therefore, if Eq. (6) is modified so to be non-dimensional with respect to I_{xx} a unique solution can be determined:

$$\left[\underline{\underline{\dot{\Omega}}}^{LRF}_{TRF/LRF}{}_m + [\boldsymbol{\omega}^{LRF}_{TRF/LRF}\times]\underline{\underline{\Omega}}^{LRF}_{TRF/LRF}{}_m\right]\boldsymbol{I}_{T,m} = 0 \tag{10}$$

In Eq. (10), the matrix $\underline{\underline{\dot{\Omega}}}^{LRF}_{TRF/LRF}{}_m$ is obtained from Eq. (9) by erasing the first column, while $\boldsymbol{I}_{T,m}$ is the vector of the MIRs, i.e., the moment of inertia adimensionalized with respect to I_{xx}.

To avoid the need of numerically computing angular accelerations (which would amplify the level of noise in the solution), the linear system is built to estimate the MIRs with the integrated form of Eq. (10):

$$[\underline{\underline{\Omega}}^{LRF}_{TRF/LRF}(t+\Delta t) - \underline{\underline{\Omega}}^{LRF}_{TRF/LRF}(t) + \int_t^{t+\Delta\tau}[\boldsymbol{\omega}^{LRF}_{TRF/LRF}\times]\underline{\underline{\Omega}}^{LRF}_{TRF/LRF}dt]\boldsymbol{I}_T = \begin{bmatrix} -\omega_x \\ 0 \\ 0 \end{bmatrix} \tag{11}$$

4. EXPERIMENTTAL SET-UP

A schematic representation of the experimental set-up is provided in Fig. 2.

The spherical air bearing provides the rotational degrees of freedom: it guarantees full 360° rotation around the vertical axis; however, the rotation around the axes parallel to the floor is limited by the presence of structural elements. The air used by the bearing is stored in two 4500 psi paintball tanks and it is stepped down to a 100 psi by pressure regulators. Then the air flows through the line which connect the tanks to the spherical cup air bearing supporting the spherical segment ball. A 3D-printed scaled-down satellite mock-up made of Acrilonitrile-Butadiene-Stirene (ABS) is attached to the bearing.

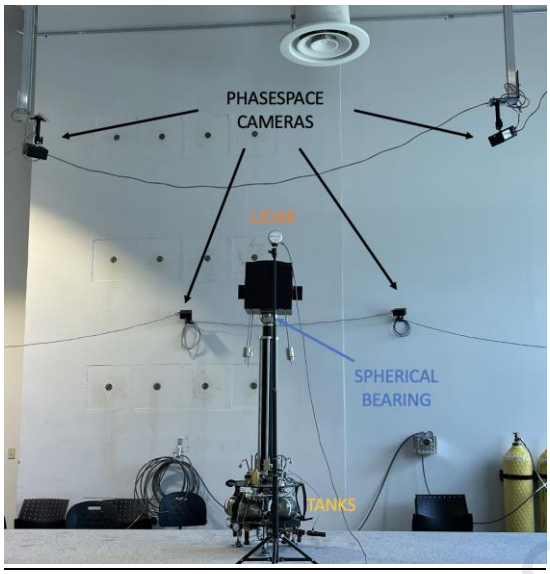

Fig. 2 Experimental set-up.

A counterbalancing system is used to minimize the gravity torque caused by the misalignment between the centre of mass of the system and the centre of rotation (which coincides with the centre of the spherical bearing). It is a passive system composed of four arms symmetrically extending downwards the 3D printed model to whose ends static weights are placed. The details of both the mock-up and counter-balancing system are shown in Fig. 3.

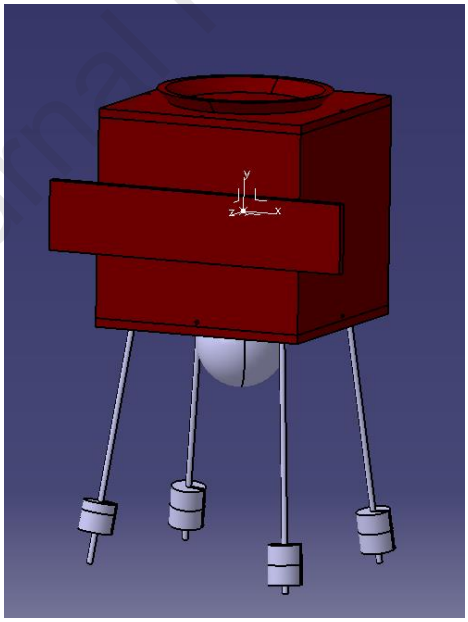

Fig. 3 CAD model of the satellite mock-up, spherical air bearing and counter-balancing system. The reference frame shown is the BRF.

The LIDAR selected as navigation sensor is the Intel RealSense LIDAR camera L515, a low-cost, high-resolution solid state LIDAR depth camera, [24]. An overview of the sensor characteristics is provided in Tab. 1.

Operational parameters		Noise parameters	
Field of View	70°x55°		2.5mm @ 1m
Resolution	1024x768	Depth standard deviation	
Frame rate	30 fps		15.5mm @ 9m

Tab. 1 Intel RealSense LIDAR camera L515 characteristics, [24].

The ground truth which allows evaluating the accuracy of the ICP-based pose estimate is provided by the PhaseSpace Impulse System: it is a motion capture system which provides the reference pose parameters of TRF with respect to MTRF. It consists of a string of eight LEDs powered by a small rechargeable battery pack imaged by a set of 12 cameras hung up around the experimental facility. The configuration of the LEDs on the spacecraft model is shown in Fig. 4.

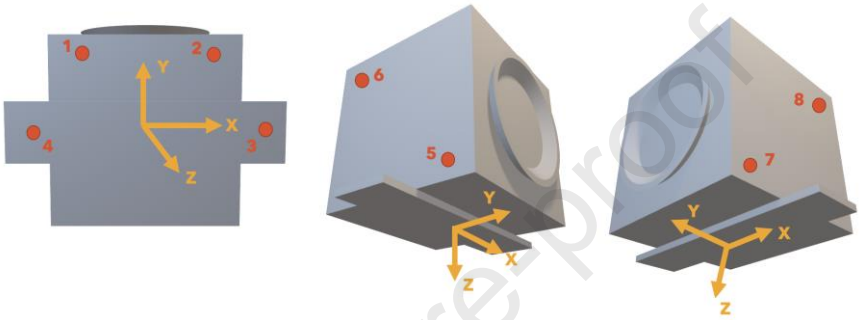

Fig. 4 Position of LEDs on the spacecraft mock-up represented by red dots. The axis shown in the figure are parallel to the ones of TRF.

Each LED blinks according to a unique pattern which make them recognizable and identifiable by the system. The cameras send the acquired data to a server through Ethernet cables which computes the position and attitude of the rigid body equipped with the LEDs with a latency of 8 ms and an accuracy of 1-5 mm [25].

5. TESTING PROCEDURE

Once the system is balanced to a satisfactory level and the spherical bearing is active, an instantaneous torque can be applied to the model and it will start rotating, simulating an almost friction and torque-free motion. While the model is rotating, the LIDAR acquires images of the scene, and the target motion is estimated through the ICP-based pose determination strategy presented in Section 3.1.

It is worth noting that the ICP requires an initial estimate of the pose parameters (pose initial guess). Since the pose initialization is not the focus of this work, the pose initial guess is obtained from the PhaseSpace data. However, to obtain the pose parameters of TRF with respect to MTRF, the position of each LEDs in TRF must be known. They can be determined by combining the knowledge of the geometry of the 3D-printed model and the position of the LEDs tracked by PhaseSpace system.

Also, the extrinsic calibration parameters (i.e., the position and attitude quaternion of LRF with respect to MTRF) must be computed to obtain the pose initial guess of TRF with respect to TRF and to compare the PhaseSpace-based and LIDAR-based pose measurements. The extrinsic calibration procedure is described in the following section.

5.1 Extrinsic calibration

Horn's absolute orientation method is applied to obtain the translation and rotation vector of LRF with respect to MTRF, [26]. It requires the knowledge of the position of at least four points in both reference frames.

To this aim a string of eight LEDs is placed on a flat panel, as shown in Fig. 5. The position of the LEDs in the MTRF are straightforward to obtain by turning on the LEDs and tracking them with PhaseSpace.

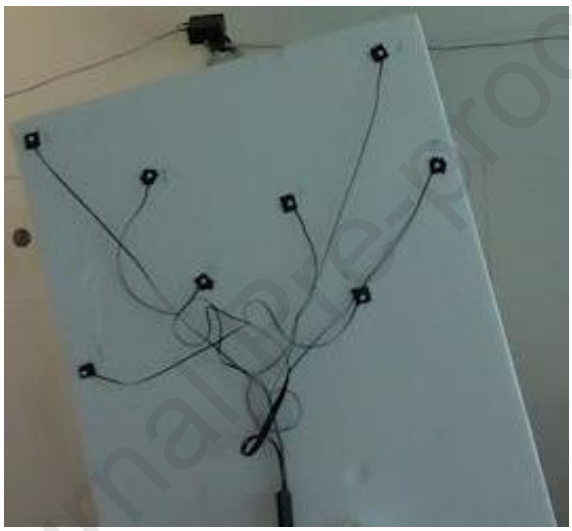

Fig. 5 Calibration object.

On the other hand, to obtain the position of the LEDs in LRF, the RGB sensor of the LIDAR L515 is exploited. Two different images of the calibration object are acquired: one with the LEDs switched on and one with the LEDs switched off. Then, by performing the pixel-wise subtraction of the corresponding grey-scale normalized images in Fig. 6 (a-b), one containing only the LEDs is obtained (see Fig. 6 (c)).

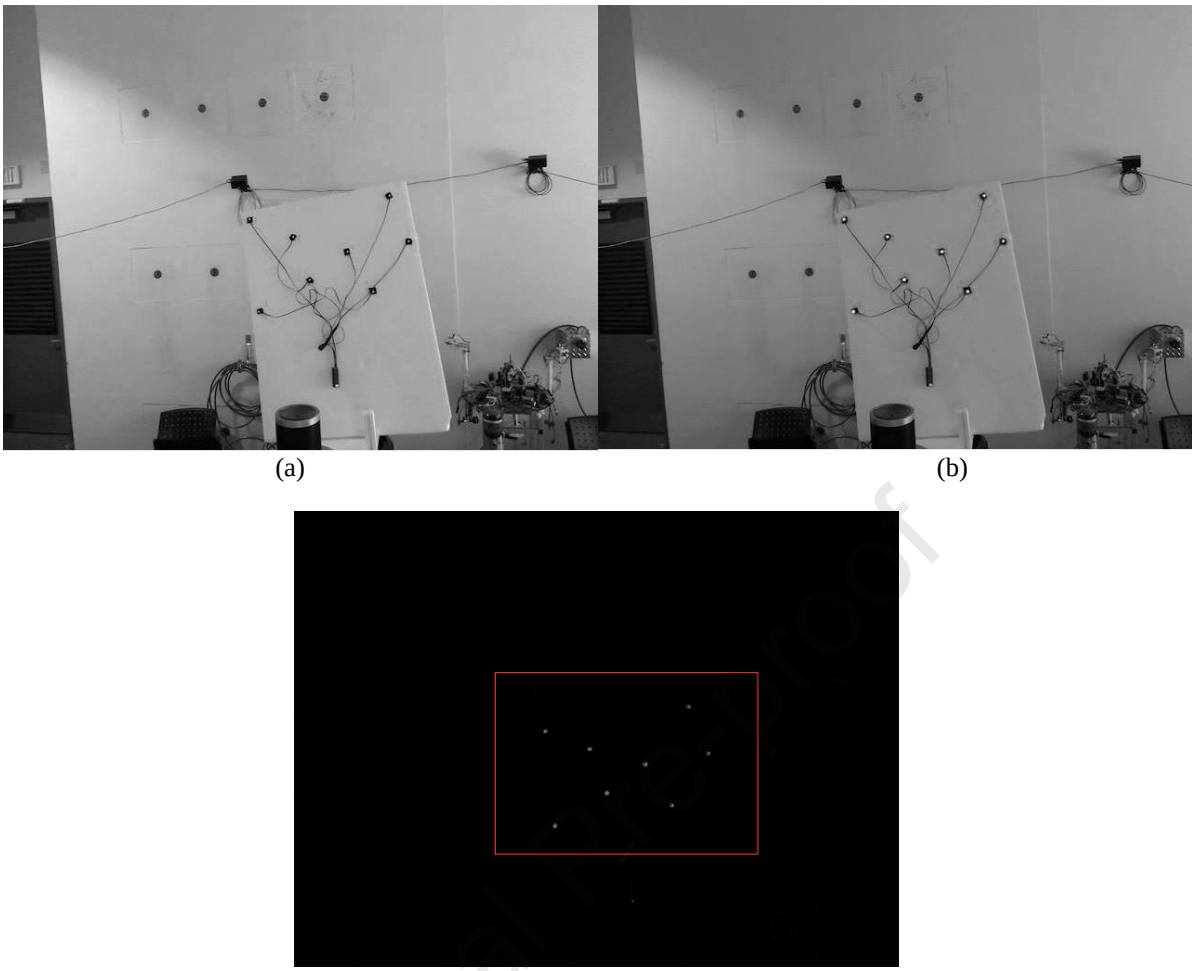

(a) (b)

(c)

Fig. 6 (a) Grey-scale image with LEDs off (b) Grey-scale image with LEDs on (c) Difference intensity image obtained subtracting the two acquired images.

The image-plane coordinates of each LEDs are obtained as the coordinates of the centroid of the blobs of pixels computed by weighting each pixel based on its intensity, as in Eq. (12):

$$U_i = \frac{\sum_{j=1}^{N} u_j I_j}{\sum_{j=1}^{N} I_j}, \quad V_i = \frac{\sum_{j=1}^{N} v_j I_j}{\sum_{j=1}^{N} I_j}, \quad i = 1,\ldots,N \tag{12}$$

where (U_I, V_i) and (u_I,v_i) are the image plane coordinates of the *i*-th blobs and of the *j*-th pixel, respectively and I_j its intensity. Then, the normalized image coordinates are obtained as follows:

$$x_{dn,i} = \frac{U_i - p_u}{f_x}, \quad y_{dn,i} = \frac{V_i - p_v}{f_y} \tag{13}$$

where f_x and f_y are the horizontal and vertical focal lengths and (p_u, p_v) are the coordinates of the camera principal point. Eq. (13) represents the distorted normalized coordinates: to obtain the undistorted ones, ($x_{n,I}$, $y_{n,i}$), the Brown Conrady distortion model must be applied to remove the radial and tangential distortion, as explained in [27]:

$$x_{n,i} = x_{dn,i}\,h + 2k_3h^2x_{dn,i}y_{dn,i} + k_4\left(r + 2x_{dn,i}^2h^2\right)$$
$$y_{n,i} = y_{dn,i}\,h + 2k_3h^2x_{dn,i}y_{dn,i} + k_4(r + 2y_{dn,i}^2h^2) \quad (14)$$

where

$$h = 1 + k_1r + k_2r^2 + k_5r^3 \quad (15)$$

$$r = \sqrt{(x_{dn,i}^2 + y_{dn,i}^2)} \quad (16)$$

and k_i is the *i*-th image distortion coefficients.

To improve the accuracy of the extrinsic calibration procedure, multiple acquisitions varying the position and orientation of the calibration object with respect to the camera are considered: this allows solving the absolute orientation problems using 24 points instead of 8. Fig. 7 shows the reprojection error of the coordinates of each LED P_i, computed with the obtained extrinsic calibration parameters ($\boldsymbol{t}_{PRF\to LRF}, \boldsymbol{q}_{LRF/PRF}$)) as in Eq. (17), while in Tab. 2 the root mean square (RMS) and maximum of $\boldsymbol{x_{err,rep}}$ are listed.

$$\boldsymbol{x_{err,rep}} = \boldsymbol{P}_i^{MTRF} - \boldsymbol{t}_{MTRF\to LRF} + R_{LRF}^{MTRF}\boldsymbol{P}_i^{LRF} \quad (17)$$

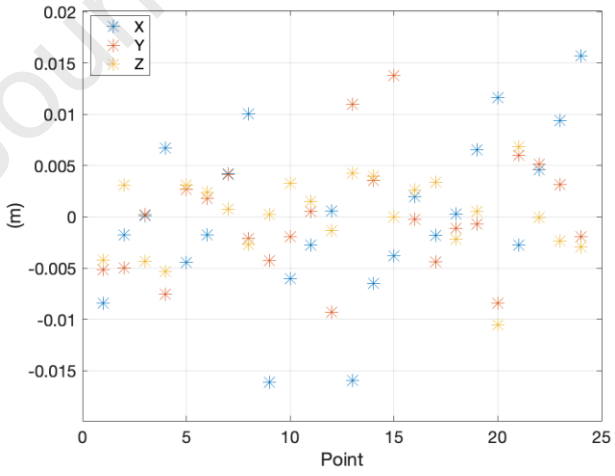

Fig. 7 Reprojection error of the points used for the extrinsic calibration.

	$\boldsymbol{x_{err,rep}}(x)$	$\boldsymbol{x_{err,rep}}\ (y)$	$\boldsymbol{x_{err,rep}}\ (z)$
RMS (m)	0.0077	0.0056	0.0038
MAX (m)	0.0161	0.0138	0.0105

Tab. 2 Statistics of the reprojection errors.

5.2 Residual gravity effect

Due to the difficulties of precisely balancing the system by moving the static weights along the balancing bars, it is not possible to obtain a perfectly gravity free-torque motion. However, the offset between the centre of gravity and the centre of rotation along with the reference value for the moment of inertia ratios, can be both estimated from the CAD model by defining the density properties of each element of the system. Also, to check possible discrepancies between the real system and the modelled ones, a modified version of the system of Eq. (11) in which the gravity torque is added and the centre of gravity (CoG)-center of rotation (CoR) offset is included in the unknown vector can be exploited:

$$[\underline{\underline{\Omega}}^{LRF}_{TRF/LRF}(t+\Delta t) - \underline{\underline{\Omega}}^{LRF}_{TRF}(t) + \int_t^{t+\Delta\tau} [\boldsymbol{\omega}^{LRF}_{TRF}\times]\underline{\underline{\Omega}}^{LRF}_{TRF}dt\,, \int_t^{t+\Delta t}[\boldsymbol{g}\times]d\tau]\left[\boldsymbol{I}_T\,;\,\frac{m\boldsymbol{r}}{I_{xx}}\right] = \begin{bmatrix}-\omega_x\\0\\0\end{bmatrix} \tag{18}$$

In Eq. (21), $\boldsymbol{g}$ is the gravity vector, m is the mass of the system and $\boldsymbol{r}$ is the centre of mass-centre of rotation offset vector. The system of Eq. (21) is solved using the data acquired by the PhaseSpace system. The results obtained from different acquisitions (denoted as PS-i) along with the values obtained from the CAD model are reported in Tab. 3.

Parameter	CAD	PS-1	PS-2	PS-3	PS-4	PS-5	PS-6
I_{yy}/I_{xx}	0.2440	0.2897	0.2938	0.2413	0.2465	0.2359	0.2741
I_{zz}/I_{xx}	0.9900	1.0040	0.9879	0.9147	0.8928	0.9563	0.9532
I_{xy}/I_{xx}	0.0096	-0.0060	0.0024	0.0060	-0.0031	-0.0072	0.0166
I_{xz}/I_{xx}	-0.0032	-0.0153	-0.0029	-0.0064	-0.0186	0.0033	0.0124
I_{yz}/I_{xx}	-0.0289	-0.0203	-0.0218	-0.0067	-0.0108	-0.0284	-0.0009
mr_x/I_{xx}	0	-0.0014	0.0041	0.0017	0.0034	0.0046	-0.0015
mr_y/I_{xx}	-0.3467	-0.3853	-0.3887	-0.3722	-0.3716	-0.3768	-0.3807
mr_z/I_{xx}	0	0.0103	0.0090	0.0107	0.0088	0.0074	0.0071

Tab. 3 MIRs and center of gravity-center of rotation offset estimated from the CAD model and PhaseSpace data.

The reason for the different results in the PhaseSpace acquisitions lies in the numerical differentiation of the quaternion to estimate the angular velocity. However, as shown in Tab. 4, the standard deviations of both the principal moment of inertia ratios (I_{yy}/I_{xx} and I_{zz}/I_{xx}) and the dimensionless CoR-CoG vertical offset are one order of magnitude lower than the estimated values. The high variability of the other parameters between the different acquisitions is due to the fact that, being very low with respect to the principal MIRs and vertical off-set, they have a negligible impact on the rotational dynamics of the system which makes their estimate highly sensitive to the measurement noise.

Parameter	Standard Deviation
I_{yy}/I_{xx}	0.0245
I_{zz}/I_{xx}	0.0412
I_{xy}/I_{xx}	0.0087
I_{xz}/I_{xx}	0.0106
I_{yz}/I_{xx}	0.0109
mr_x/I_{xx}	0.0026
mr_y/I_{xx}	0.0138
mr_z/I_{xx}	0.0036

Tab. 4 Standard deviation of MIRs and CoG-CoR offset.

It is worth underlining that the gravity torque term is only needed to counteract the fact that the system is not perfectly balanced. In an ideal case in which the centre of gravity and of rotation are coincident, the only perturbation acting on the model is due to the friction between the spherical bearing cup and segment ball which has a negligible effect [28].

Moreover, in order to verify the accuracy of the CAD model of the system, the moments of inertia of both spacecraft mock-up and spherical air bearing has been measured with the K-KOC Moment of Inertia and Mass Properties Measurement System from Karakamlar [29], as shown in Fig. 8, and compared with the ones derived from the CAD model.

(a)

(b)

Fig. 8 Moments of inertia measurements with K-KOC moment of inertia and mass properties measurement system: (a) spacecraft mock-up, (b) spherical air bearing.

To reduce the uncertainties, multiple measurements have been performed whose mean and standard deviation are reported in Table 5. The mean % difference of the mean value obtained from the K-KOC machine with respect to the one obtained from the CAD model is 1.2%.

	Parameter	Mean	Standard Deviation
Spacecraft Mock-up	I_{xx}	1238.36	2.25
	I_{yy}	1201.22	2.25
	I_{zz}	686.08	1.74
Spherical Air Bearing	I_{xx}	28.47	0.93
	I_{yy}	28.66	0.93
	I_{zz}	28.14	1.09

Tab. 5 Statistics of the inertia measurements with K-KOC machine.

6. TEST RESULTS

Before introducing and discussing the experimental results, the performance metrics adopted to evaluate the accuracy of both ICP and MIRs estimation algorithm are defined. The attitude performance metrics of the ICP-based pose determination algorithm are the angular deviations between the reference (i.e., PhaseSpace data) and the estimated direction of TRF in LRF computed as in Eq. (19):

$$\begin{aligned} e_{x,dir} &= \cos^{-1}(\underline{\underline{R}}_{1,EST}, \underline{\underline{R}}_{1,TRUE}) \\ e_{y,dir} &= \cos^{-1}(\underline{\underline{R}}_{2,EST}, \underline{\underline{R}}_{2,TRUE}) \\ e_{z,dir} &= \cos^{-1}(\underline{\underline{R}}_{3,EST}, \underline{\underline{R}}_{3,TRUE}) \end{aligned} \tag{19}$$

where $\underline{\underline{R}}_i$ is the *i*-th column of the rotation matrix representing the attitude of TRF with respect to LRF. Regarding the moment of inertia ratios, the error metric is defined as follows:

$$\boldsymbol{I}_{ERR} = \frac{|\boldsymbol{I}_{REF} - \boldsymbol{I}_{EST}|}{\boldsymbol{I}_{REF}} \tag{20}$$

where $\boldsymbol{I}_{REF}$ is the vector containing the mean values among the reference solutions obtained by the PhaseSpace-based test and from the CAD model (listed in Tab. 3).

As described in Section 3, the first step is to obtain attitude and angular velocity estimates by processing the acquired point clouds. The time variation of the attitude performance metrics for the test case presented in this work is depicted in Fig. 9, while their statistics are listed in Tab. 6.

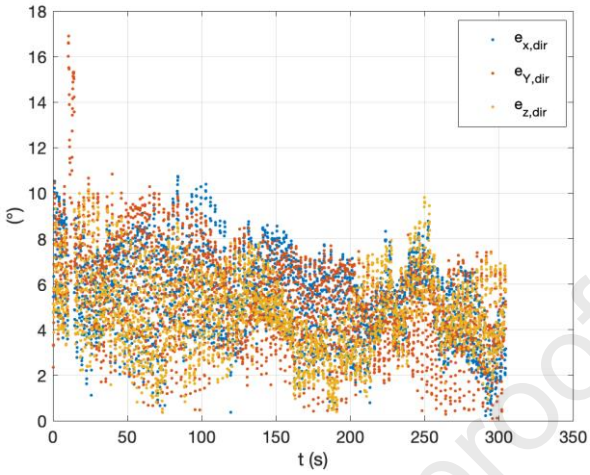

Fig. 9 Time variation of the performance metrics defined for the relative attitude.

Metrics	Mean (°)	Standard Deviation (°)
$e_{x,dir}$	5.312	1.897
$e_{y,dir}$	5.299	2.23
$e_{z,dir}$	4.686	1.775

Tab. 6 Statistics of the performance metrics defined for the relative attitude.

It is worth outlining that the errors of the ICP-based pose determination algorithm include, along with the errors related to the limited accuracy of the sensors, the calibration errors (cm-level error) and the tracking errors of the PhaseSpace system. These latter errors include two contributions: the errors in the tracking of each LED and the uncertainty due to the imperfect knowledge of their positions in TRF.

Once attitude information is collected, the angular velocity of the system is estimated through Eq. (4). Since the estimate of the angular velocity must be as accurate as possible to obtain a good estimate of the MIRs, the time interval over which the rotation angle $\boldsymbol{\varphi}$ must be computed is not constant but it is chosen taking into account the accuracy of the estimated pose provided by the value of the ICP cost function at the last iteration, f_{END}. Thus, the numerical derivative of $\boldsymbol{\varphi}$ is computed only if the value of f_{END} is lower than a user defined threshold.

With the estimated values of attitude and angular velocity, along with the CoG-CoM offset provided by the CAD model, Eq. (21) (obtained from Eq. (19) considering the gravity torque a known term) is exploited to obtain an estimate of the MIRs whose results are summarized in Tab. 7:

$$[\underline{\underline{\Omega}}^{LRF}_{TRF/LRF}(t+\Delta t) - \underline{\underline{\Omega}}^{LRF}_{TRF/LRF}(t) + \int_t^{t+\Delta\tau} [\boldsymbol{\omega}^{LRF}_{TRF/LRF}\times]\underline{\underline{\Omega}}^{LRF}_{TRF/LRF}dt]\boldsymbol{I}_T = \begin{bmatrix} -\omega_x \\ 0 \\ 0 \end{bmatrix} - \int_t^{t+\Delta\tau} \frac{m[\boldsymbol{g}\times]\boldsymbol{r}}{I_{xx}}dt \quad (21)$$

MIRs	Reference values	Estimated values	Performance metrics
I_{yy}/I_{xx}	0.2680	0.2186	19%
I_{zz}/I_{xx}	0.9570	1.0751	10.46%

Tab. 7 Estimation error of principal MIRs.

It is important to underline that the results provided in Tab. 7 are not only influenced by the uncertainty on the angular velocity estimate, but they also depend on the accuracy on the knowledge of the gravity torque (i.e., CoG-CoM offset) and I_{xx}_terms added to Eq. (11) to counteract the effect of an imperfectly balanced system and derived from the CAD model. The performance of the algorithm is expected to improve with a more accurate knowledge of the system parameters and by integrating an active balancing system able to align perfectly the CoR with the CoG.

7. CONCLUSIONS

This paper presented the experimental validation of an algorithmic architecture for the estimation of the attitude and moment of inertia ratios of a non-cooperative freely tumbling spacecraft which exploits the measurements of a solid-state LIDAR. Specifically, the attitude is estimated by processing the acquired 3D point clouds with a customized version of the Iterative Closest Point algorithm, while the MIRs are estimated by solving a linear system based on the integral form of the Euler equation. Along with the solid-state LIDAR, the experimental set-up built to validate the performance of the algorithm includes a scaled down satellite mock-up which can rotate as an almost torque-free rigid body thanks to a spherical air bearing and a counter-balancing system and a motion tracking system to be used as benchmark for the estimated attitude. The presented test case shows that the ICP allows estimating the attitude with a mean error of 5° and a standard deviation of 2°, while the principal moment of inertia can be estimated with an accuracy lower than 20%.

Future works will assess the MIRs and attitude estimation performance by considering various target in terms of geometries and rotational dynamics by eliminating the limitation imposed by the spherical air bearing.

Acknowledgements

The stay of Alessia Nocerino at Embry Riddle Aeronautical University was financially supported by UniNA and Compagnia di San Paolo, in the frame of Programme STAR PLUS. The research activity was financially supported by the Advanced Autonomous Multiple Spacecraft laboratory of Embry Riddle Aeronautical University.

REFERENCES

[1] "https://orbitaldebris.jsc.nasa.gov/library/iadc-space-debris-guidelines-revision-2.pdf."

[2] H. Klinkrad *et al.*, "The ESA Space Debris Mitigation Handbook 2002," *Advances in Space Research*, vol. 34, no. 5, pp. 1251–1259, 2004, doi: https://doi.org/10.1016/j.asr.2003.01.018.

[3] J.-C. Liou and N. L. Johnson, "A sensitivity study of the effectiveness of active debris removal in LEO," *Acta Astronaut*, vol. 64, no. 2, pp. 236–243, 2009, doi: https://doi.org/10.1016/j.actaastro.2008.07.009.

[4] H. G. Lewis, A. E. White, R. Crowther, and H. Stokes, "Synergy of debris mitigation and removal," *Acta Astronautica*, vol. 81, no. 1, pp. 62–68, 2012, doi: https://doi.org/10.1016/j.actaastro.2012.06.012.

[5] J.-C. Liou, N. L. Johnson, and N. M. Hill, "Controlling the growth of future LEO debris populations with active debris removal," *Acta Astronaut*, vol. 66, no. 5, pp. 648–653, 2010, doi: https://doi.org/10.1016/j.actaastro.2009.08.005.

[6] Q. Meng, J. Liang, and O. Ma, *Estimate of All the Inertial Parameters of a Free-Floating Object in Orbit*. 2018. doi: 10.2514/6.2018-1606.

[7] Q. Meng, C. Zhao, H. Ji, and J. Liang, "Identify the full inertial parameters of a non-cooperative target with eddy current detumbling," *Advances in Space Research*, 2020, doi: https://doi.org/10.1016/j.asr.2020.05.044.

[8] D. Sheinfeld and S. Rock, "Rigid body inertia estimation with applications to the capture of a tumbling satellite," in *Proceedings of 19th AAS/AIAA spaceflight mechanics meeting*, 2009, vol. 134, pp. 343–356.

[9] H. Benninghoff and T. Boge, *Rendezvous Involving a Non-Cooperative, Tumbling Target - Estimation of Moments of Inertia and Center of Mass of an Unknown Target*. 2015.

[10] S. Segal, A. Carmi, and P. Gurfil, "Stereovision-Based Estimation of Relative Dynamics Between Noncooperative Satellites: Theory and Experiments," *Control Systems Technology, IEEE Transactions on*, vol. 22, pp. 568–584, Mar. 2014, doi: 10.1109/TCST.2013.2255288.

[11] H. Yu, X. Zhang, L. Liu, S. Wang, and S. Song, "Relative dynamics estimation of non-cooperative spacecraft with unknown orbit elements and inertial tensor," *Chinese Journal of Aeronautics*, vol. 29, no. 2, pp. 479–491, 2016, doi: https://doi.org/10.1016/j.cja.2016.01.013.

[12] X. Wang, Z. Wang, and Y. Zhang, "Stereovision-based relative states and inertia parameter estimation of noncooperative spacecraft," *Proc Inst Mech Eng G J Aerosp Eng*, vol. 0, no. 109, pp. 1–14, 2018, doi: 10.1177/0954410018782021.

[13] B.-Z. Zhou, G.-P. Cai, Y.-M. Liu, and P. Liu, "Motion prediction of a non-cooperative space target," *Advances in Space Research*, vol. 61, no. 1, pp. 207–222, 2018, doi: https://doi.org/10.1016/j.asr.2017.10.028.

[14] B. Tweddle, "Computer vision-based localization and mapping of an unknown, uncooperative and spinning target for spacecraft proximity operations," Mar. 2014.

[15] V. Pesce, M. Lavagna, and R. Bevilacqua, "Stereovision-based pose and inertia estimation of unknown and uncooperative space objects," *Advances in Space Research*, vol. 59, no. 1, pp. 236–251, 2017, doi: 10.1016/j.asr.2016.10.002.

[16] D. Ivanov, M. Ovchinnikov, and M. Sakovich, "Relative Pose and Inertia Determination of Unknown Satellite Using Monocular Vision," *International Journal of Aerospace Engineering*, Sep. 2018, doi: 10.1155/2018/9731512.

[17] F. Aghili and K. Parsa, "Motion and Parameter Estimation of Space Objects Using Laser-Vision Data," *Journal of Guidance Control and Dynamics - J GUID CONTROL DYNAM*, vol. 32, pp. 538–550, Mar. 2009, doi: 10.2514/1.37129.

[18] M. Lichter and S. Dubowsky, *State, Shape, and Parameter Estimation of Space Objects from Range Images*. 2004. doi: 10.1109/ROBOT.2004.1307513.

[19] Y. Li, Y. Wang, and Y. Xie, "Using consecutive point clouds for pose and motion estimation of tumbling non-cooperative target," *Advances in Space Research*, vol. 63, no. 5, pp. 1576–1587, 2019, doi: https://doi.org/10.1016/j.asr.2018.11.024.

[20] A. Nocerino, R. Opromolla, G. Fasano, and M. Grassi, "LIDAR-based multi-step approach for relative state and inertia parameters determination of an uncooperative target," *Acta Astronautica*, vol. 181, pp. 662–678, 2021, doi: https://doi.org/10.1016/j.actaastro.2021.02.019.

[21] P. J. Besl and N. D. McKay, "A method for registration of 3-D shapes," *IEEE Trans Pattern Anal Mach Intell*, vol. 14, no. 2, pp. 239–256, 1992, doi: 10.1109/34.121791.

[22] R. Opromolla, G. Fasano, G. Rufino, and M. Grassi, "Pose Estimation for Spacecraft Relative Navigation Using Model-Based Algorithms," *IEEE Trans Aerosp Electron Syst*, vol. Vol. 53, pp. 431–447, Jan. 2017, doi: 10.1109/TAES.2017.2650785.

[23] R. W. Schafer, "What Is a Savitzky-Golay Filter? [Lecture Notes]," *IEEE Signal Processing Magazine*, vol. 28, no. 4, pp. 111–117, 2011, doi: 10.1109/MSP.2011.941097.

[24] "https://www.intelrealsense.com/lidar-camera-l515/."

[25] K. Saulnier, D. Pérez, R. C. Huang, D. Gallardo, G. Tilton, and R. Bevilacqua, "A six-degree-of-freedom hardware-in-the-loop simulator for small spacecraft," *Acta Astronaut*, vol. 105, no. 2, pp. 444–462, 2014, doi: https://doi.org/10.1016/j.actaastro.2014.10.027.

[26] B. K. P. Horn, "Closed-form solution of absolute orientation using unit quaternions," *Journal of the Optical Society of America A*, vol. 4, no. 4, pp. 629–642, 1987, doi: 10.1364/JOSAA.4.000629.
[27] "https://dev.intelrealsense.com/docs/projection-texture-mapping-and-occlusion-with-intel-realsense-depth-cameras#6-appendix-1---distortion-models."
[28] J. L. Schwartz, M. A. Peck, and C. D. Hall, "Historical Review of Air-Bearing Spacecraft Simulators," *Journal of Guidance, Control, and Dynamics*, vol. 26, no. 4, pp. 513–522, Jul. 2003, doi: 10.2514/2.5085.
[29] "Moment of Inertia Measurement System | PRODUCTS & SERVICES." https://www.karakamlar.com/urunler/moment-of-inertia.html (accessed Jan. 26, 2023).

Highlights:

- The estimation of attitude and inertia parameters of an uncooperative space target is addressed.
- A LIDAR-based algorithmic architecture is experimentally validated.
- The design and calibration of the experimental set-up is described.
- Errors below 10° and 20% are obtained for attitude and inertia parameter, respectively.

Declaration of interests

☒ The authors declare that they have no known competing financial interests or personal relationships that could have appeared to influence the work reported in this paper.

☐The authors declare the following financial interests/personal relationships which may be considered as potential competing interests: